Vertical Distribution of Aerosols and Hazes Over Jupiter's Great Red Spot and Its Surroundings in 2016 From HST/WFC3 Imaging

Asier Anguiano-Arteaga[1] [iD], Santiago Pérez-Hoyos[1] [iD], Agustín Sánchez-Lavega[1] [iD], José Francisco Sanz-Requena[2,3] [iD], and Patrick G. J. Irwin[4] [iD]

[1]Departamento de Física Aplicada, EIB, Universidad del País Vasco UPV/EHU, Bilbao, Spain, [2]Departamento de Ciencias Experimentales, Universidad Europea Miguel de Cervantes, Valladolid, Spain, [3]Departamento de Física Teórica, Atómica y Óptica, Universidad de Valladolid, Valladolid, Spain, [4]Atmospheric, Oceanic and Planetary Physics, Department of Physics, University of Oxford, Oxford, UK

Abstract In this work, we have analyzed images provided by the Hubble Space Telescope's Wide Field Camera 3 (HST/WFC3) in December 2016, with a spectral coverage from the ultraviolet to the near infrared. We have obtained the spectral reflectivity of the GRS and its surroundings, with particular emphasis on selected, dynamically interesting regions. A spectral characterization of the GRS area is performed following two different procedures: (a) in terms of Altitude/Opacity and Color Indices (AOI and CI); (b) by means of automatic spectral classification. We used the NEMESIS radiative transfer suite to retrieve the main atmospheric parameters (e.g., particle vertical and size distributions, refractive indices) that are able to explain the observed spectral reflectivity. The optimal *a priori* model atmosphere used for the retrievals is obtained from a grid of about 12,000 different atmospheric models, and choosing the one that best fits South Tropical Zone (STrZ) spectra and its observed limb-darkening. We conclude that the spectral reflectivity of the GRS area is well reproduced with the following layout: (a) a stratospheric haze with its base near the 100 mbar level, with optical depths at 900 nm of the order of unity and particles with a size of 0.3 μm; (b) a more vertically extended tropospheric haze, with τ (900 nm) ~10 down to 500 mbar and micron sized particles. Both haze layers show a stronger short wavelength absorption, and thus both act as chromophores. The altitude difference between clouds tops in the GRS and surrounding areas is ~10 km.

Plain Language Summary One of the main questions concerning the Great Red Spot (GRS) of Jupiter is the origin of its reddish color. It is commonly understood that the cause of this feature are one or more unknown species of aerosols located in the upper atmosphere. Even in the whitest areas of Jupiter, stronger blue light absorption has been measured, suggesting the global presence of one or more species of blue absorbing aerosols. We use Hubble Space Telescope (HST) observations to retrieve atmospheric models describing the vertical structure and some of the main atmospheric properties of the hazes in the GRS and its surrounding area. Our results suggest that two different blue absorbing aerosols are able to account for the color of the GRS and its vicinity.

1. Introduction

The Great Red Spot of Jupiter is one of the most intriguing atmospheric phenomena in the solar system. Although it has been widely studied in detail in the past decades (Dowling & Ingersoll, 1989; Flasar et al., 1981; Sada et al., 1996) and recent years (Baines et al., 2019; Sánchez-Lavega et al., 2018, 2021; Simon et al., 2018), many unknowns remain. One of the main questions is its reddish coloration, which is directly related to the vertical distribution and composition of the hazes and clouds in upper atmospheric levels (*P* < 1 bar). In fact, the different colorations throughout Jupiter are expected to be explained in terms of such variables. Several works have studied this problem analyzing the spectra of the GRS, mainly working in the visible (Baines et al., 2019; Braude et al., 2020; Sromovsky et al., 2017), and infrared ranges (De Pater et al., 2010; Grassi et al., 2021). In order to explain the strong short-wavelength absorption in the GRS, Carlson et al. (2016) proposed a coloring agent resulting from photolyzed ammonia reacting with acetylene. In this scheme, the GRS color would be the result of vertical motions in the GRS that lift material to the upper troposphere or

lower stratosphere, allowing the photochemical reactions that lead to the creation of the coloring agent. Sromovsky et al. (2017) affirmed that this agent could act as a universal chromophore and, as well as Baines et al. (2019), they were able to satisfactorily reproduce the GRS spectra under different observing geometries with data obtained by the Cassini VIMS instrument. However, Simon-Miller et al. (2001a) and Ordonez-Etxeberria et al. (2016) had previously concluded from Principal Component Analysis (PCA) that the presence of of at least two coloring species was required to explain the diversity of colors in all of Jupiter's upper clouds. Pérez-Hoyos et al. (2020) and Braude et al. (2020) independently showed that a chromophore with steeper blue absorption is more suitable to account for their measured North Temperate Belt and GRS spectra, respectively. However, they did not discard the possibility of a universal chromophore to account for the different cloud colors on Jupiter. Notably, such works put an extra effort on explaining the limb-darkening of Jovian red features, under different observing and illumination geometries.

The red coloration of some dynamically relevant atmospheric features in Jupiter suggests a correlation with local dynamics. Worthy of note in this respect is the anticyclone BA, which suffered a color change from white to red (Pérez-Hoyos et al., 2009) between 2005 and 2006. Nevertheless, no considerable change in height or dynamics was observed (Hueso et al., 2009; Wong et al., 2011). Also regarding oval BA, a circulation dynamical model was proposed by de Pater et al. (2010) in order to explain the presence of a red ring covering the outer part of the oval. On the other hand, the change in the coloration of belts and zones in Jupiter has also been previously analyzed following intense dynamical perturbations (Pérez-Hoyos et al., 2020; Pérez-Hoyos, Sanz-Requena, Barrado-Izagirre, et al., 2012). These variations occur with a certain frequency, but, as with the oval BA, no persistent dynamical changes have been associated with such color modifications. Thus, the relation between dynamics and color variations is still an open subject of research.

In this study, we study spectra of the GRS and its surroundings in 2016 in order to characterize the upper clouds and aerosol properties and vertical distribution in a number of dynamically selected regions in the GRS area. The analyzed spectra are measured from high spatial resolution HST/WFC3 images, and then relevant atmospheric parameters are retrieved by means of the NEMESIS radiative transfer suite (Irwin et al., 2008). An advantage of such a set of images is that it includes images taken in the UV that, together with two methane bands of different depths, allow a high sensitivity to the vertical location of particles in levels at or around the tropopause (e.g., Pérez-Hoyos, Sanz-Requena, Barrado-Izagirre, et al., 2012, Pérez-Hoyos, Sanz-Requena, Sánchez-Lavega, et al., 2012). The high-resolution imaging also allows us to investigate the limb-darkening behavior, in particular for zonally homogeneous regions.

The study is organized as follows. In Section 2, we describe the HST/WFC3 images and the photometric calibration procedure. In Section 3, we briefly review the regions selected for analysis. We also present the method to construct the studied spectra, as well as a preliminary spectral analysis of the GRS area. In Section 4, we describe the radiative transfer modeling procedure, and the retrieved atmospheric models for each selected region. Section 5 shows the discussion of the results shown in Section 4. Finally, in Section 6 we summarize the main conclusions of this work.

2. HST/WFC3 Observations

The high spatial resolution images used in this work were taken with the Wide Field Camera 3 onboard the Hubble Space Telescope (Dressel, 2021). These images cover a wavelength range from 200 to 900 nm in eight filters, encompassing the UV region, dominated by Rayleigh scattering and chromophore absorption, and the visible continuum, as well as two methane bands of different depths located at 727 and 889 nm. Images taken with the FQ750N filter were initially considered, but later discarded as they showed systematic saturation at some latitudes. This set of filters is sensitive to the particle distribution in the upper troposphere and lower stratosphere of Jupiter (Pérez-Hoyos et al., 2020; Wong et al., 2011). The spatial resolution was approximately 160 km/pixel, allowing the analysis of selected regions according to the cloud morphology. A brief summary of the observations is shown in Table S1 in Supporting Information S1.

The images were photometrically calibrated in absolute reflectivity (Dressel, 2021), specifically in I/F (Sánchez-Lavega, 2011), and projected into planispheres with the LAIA software, similarly to previous works involving HST/WFC3 images (Pérez-Hoyos, Sanz-Requena, Barrado-Izagirre, et al., 2012; Sanz-Requena

et al., 2019). For the planisphere construction, the images were sampled to a 0.1°/pixel resolution in Jovian coordinates. A photometric cross-calibration process was performed to reduce the dispersion in *I/F* among different HST visits (Text S1 in Supporting Information S1).

Subsequently, all the planispheres in which the GRS is present were cropped covering the same region around it. The cropped planispheres have a latitudinal extent of 40° (400 pixels) and a longitudinal extent of 50° (500 pixels), and they cover latitudes from 0° to 40°S. An example planisphere for each filter is shown in Figure 1. Since the time interval of the observations approximately spans only two Jupiter rotations, most of the morphology of the GRS and its surroundings shows no major differences.

3. Analysis

The planispheres in Figure 1 show that the GRS and its surroundings present a high diversity of cloud morphologies and wavelength-dependent reflectivity that reveals differences in the vertical distribution and properties of aerosols from one area to another. Their characterization is fundamental for a proper understanding of the underlying dynamics. In this section, we present our selection of a number of key regions from both a dynamical and a spectral point of view, in order to provide a complete description of the area.

3.1. Region Selection

We first determine the regions in the GRS area with the strongest interest from a dynamical point of view according to the cloud morphology and known dynamics (see e.g., Sánchez-Lavega et al., 2018, 2021, Figure 1).

- Region 0 / GRS Nucleus: A striking feature of the GRS is the darker coloration at the core of the reddish oval (Simon et al., 2018). Wind measurements show this is a turbulent region with possible cyclonic circulation in its interior (Sánchez-Lavega et al., 2018).
- Region 1 / GRS red oval: The reddish GRS oval is a consequence of the strong absorption of ultraviolet and blue wavelengths by chromophore species whose composition is still under discussion.
- Region 2 / Convective storms: In the area northwest of the GRS, located at the South Equatorial Belt (SEB), eruptions of bright clouds due to moist convection (Hueso et al., 2002) occur with relatively high frequency (Gierasch et al., 2000; Ingersoll et al., 2000). They become sheared apart in time scales of a few days.
- Region 3 / "Hollow": Surrounding the red oval, there is an asymmetric ring of white clouds known as the "collar." The northern flank of the collar (broader than the southern one) is commonly known as the "hollow" (J. H. Rogers, 1995; Sánchez-Lavega et al., 2018). The measured wind field shows that it is part of the anticyclonic circulation of the GRS (Sánchez-Lavega et al., 2021).
- Region 4 / Stagnation region: Approximately located at 20°S and east of the GRS, there is a westward jet ($u \approx -60$ ms^{-1}) (J. H. Rogers, 1995) carrying low-albedo clouds that circulate around the GRS. However, the circulation around the hollow sometimes presents a discontinuity in the northern limit of the flow. When this occurs, the low-albedo clouds reduce their speeds at the limit of the discontinuity and form a singular region that we call the stagnation region (Sánchez-Lavega et al., 2021).
- Region 5 / STrZ 1: The South Tropical Zone (STrZ) is one of the brightest zones of Jupiter. Despite being bright and white, analyzed spectra show that blue-wavelength absorption by upper atmosphere aerosols is also present in the STrZ.
- Region 6 / STrZ 2: As explained later in Section 3.4, automatic spectral classification of the cropped planispheres shows a differentiation of the STrZ into two different spectral groups.
- Region 7 / "Lacrimal gland": This is the region of dark clouds southeast of the GRS and located at approximately latitude 25°S. This region has been recently of particular interest as it was the way out (along with the GRS eastern flank) for reddish material (the so called "flakes") ripped off the GRS by its interaction with smaller anticyclones (Sánchez-Lavega et al., 2021).
- Region 8 / "Chimney": It is located approximately at 12°S in the northern part of the GRS where it shows as a discontinuity in the low-albedo clouds that allows the material circulating around the GRS to escape from the hollow (J. H. Rogers, 2019). This material is subsequently carried eastward by the SEB zonal flow (Sánchez-Lavega et al., 2021). Although this feature was present in the current study, this is
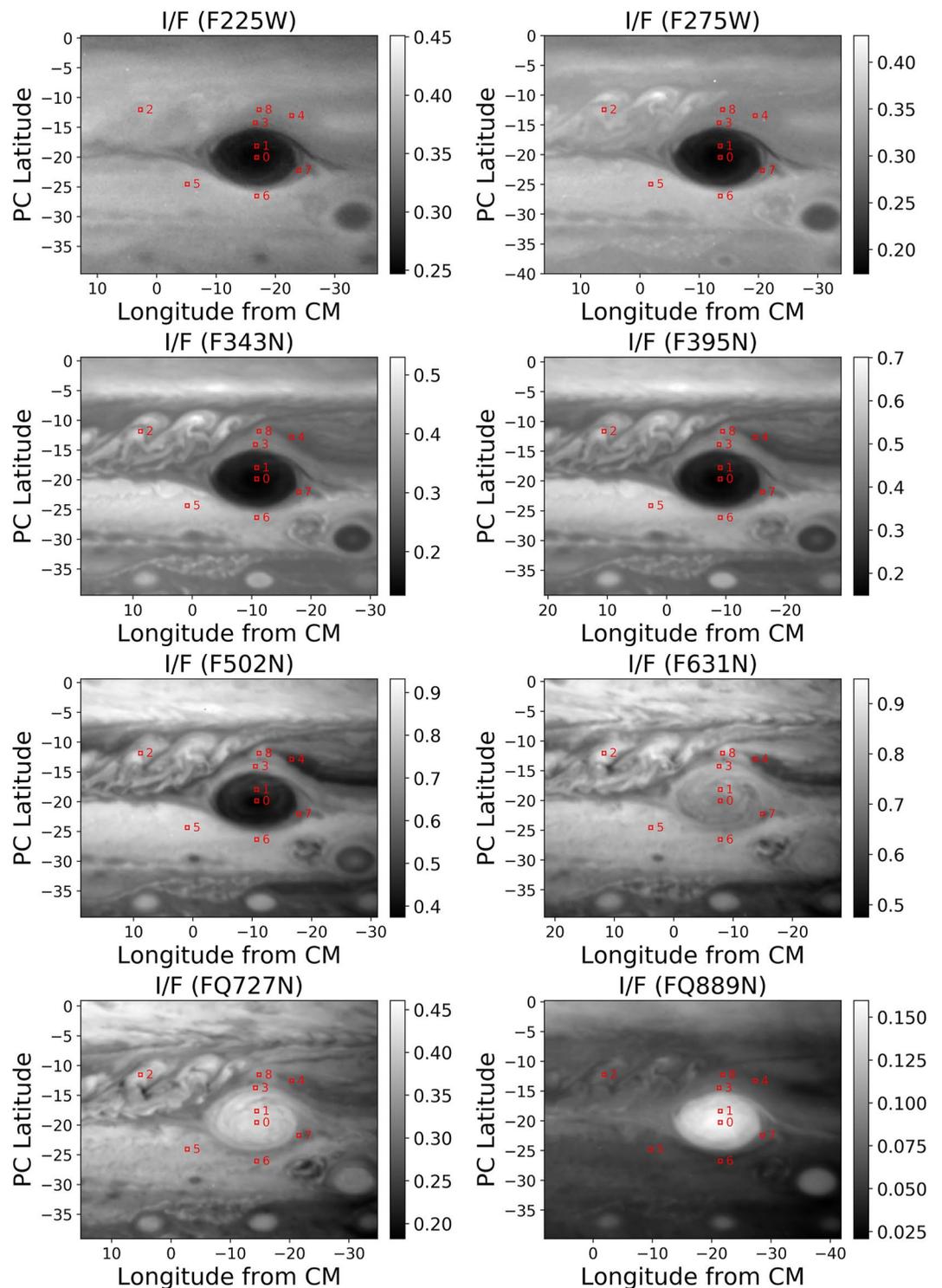
Figure 1. Cropped planispheres (0.1°/pixel resolution) showing the Great Red Spot and surroundings at the same position at different wavelengths identified by the filter name. The original images were taken between December 11 and 12, 2016. The reflectivity scale I/F is given to the right of each map. Each planisphere shows the nine regions selected for further radiative transfer analysis. Each region spans an area of 0.5° × 0.5°. A schematic wind field of the area covered by the planispheres is shown in Figure S3.

not always the case. When this happens, the north circulation surrounding the GRS is restored and the region 4 no longer shows the braking and accumulation of material.

3.2. Spectra Construction

The spectra were obtained for each region of interest and for different observing geometries. We first identified the longitudes relative to the central meridian around which the GRS is present in the largest possible number of images and in all the filters. From here on, these longitudes will be referred as "grouping longitudes," and we found them to be 60°W, 39°W, and 15°E. After that, we constructed the spectra by performing a weighted average of the I/F values of the same filter images in which the GRS center is located in ±10° from the grouping longitudes. We use weights given by a Gaussian curve centered at the grouping longitudes and with FWHM = 5° and unity peak value. The resulting spectra are shown in Figure 2.

3.3. Color Analysis

The color characterization provides a fast way to differentiate aerosol properties and/or distribution. A useful technique to get an intuitive idea of the distinction of different areas was introduced in Sánchez-Lavega et al. (2013) by obtaining two different reflectivity ratios that provide a relative measure of color and altitude/opacity, the Color Index (CI) and Altitude/Opacity Index (AOI), defined as

$$\text{CI} = \frac{I/F\left(F395N\right)}{I/F\left(F631N\right)} \tag{1}$$

$$\text{AOI} = \frac{I/F\left(FQ889N\right)}{I/F\left(F275W\right)} \tag{2}$$

Following this definition, red features will have low CI values and white-blue features will have high CI values. Similarly, high altitude features will have high AOI values, since these features are bright in the methane absorption bands and dark in the UV (the shorter atmospheric path reduces Rayleigh scattering). However, the AOI is not only sensitive to haze altitude, but also to the haze abundance/optical depth.

Using Equations 1 and 2, we made maps of AOI and CI showing the selected regions, and an AOI versus CI diagram (Figure 3) with the values of each region. In the diagram, errors in both axes are assumed to be of 10%, as this is the typical value in HST/WFC3 absolute calibration (Dressel, 2021). Since each planisphere has a different observing geometry and is affected differently by limb-darkening effects, before making these plots some geometric corrections were required. For every filter excepting F275W, the pixel I/F values were corrected following a Lambert law (Ordonez-Etxeberria et al., 2016). In the case of the F275W filter, we found that this procedure was not accurate, probably because of the strength of Rayleigh scattering close to the limb. So, in order to correct the F275W I/F values, we perform a Minnaert correction (Sánchez-Lavega, 2011), similarly as done by Ordonez-Etxeberria et al. (2016):

$$\left(\frac{I}{F}\right)_0 = \frac{\left(\frac{I}{F}\right)}{\mu_0^k \mu^{k-1}} \tag{3}$$

where k is the limb-darkening coefficient, μ_0 the cosine of the illumination angle and μ the cosine of the viewing angle. The μ_0 and μ values in the cropped planispheres used for the construction of the maps range from 0.56 to 1.0 and from 0.64 to 1.0, respectively. The limb-darkening coefficient k is calculated from the complete planispheres by performing a linear fit that obeys Equation 3 for every pixel inside the 10°–30°S range of latitudes and covering the whole longitude extent. Following this procedure, we obtained $k = 0.6$.

From the maps in Figure 3 it is possible to see that the red oval of the GRS is singular in terms of both AOI and CI. On the one hand, its high AOI values directly show that the upper clouds/hazes over the red oval are located higher in the atmosphere, or have a larger optical depth, when compared to its surroundings. On the other hand, its low CI values means that it is redder, as can be deduced from color images. This is also clear in the AOI versus CI diagram in Figure 3, where the red oval points are highly deviated from the other region values. The rest of the regions have CI in the range 0.45–0.75 CI and AOI in the range 0.15–0.4. The AOI map shows that the SEB and STrZ upper hazes might be located at similar altitudes, except the areas
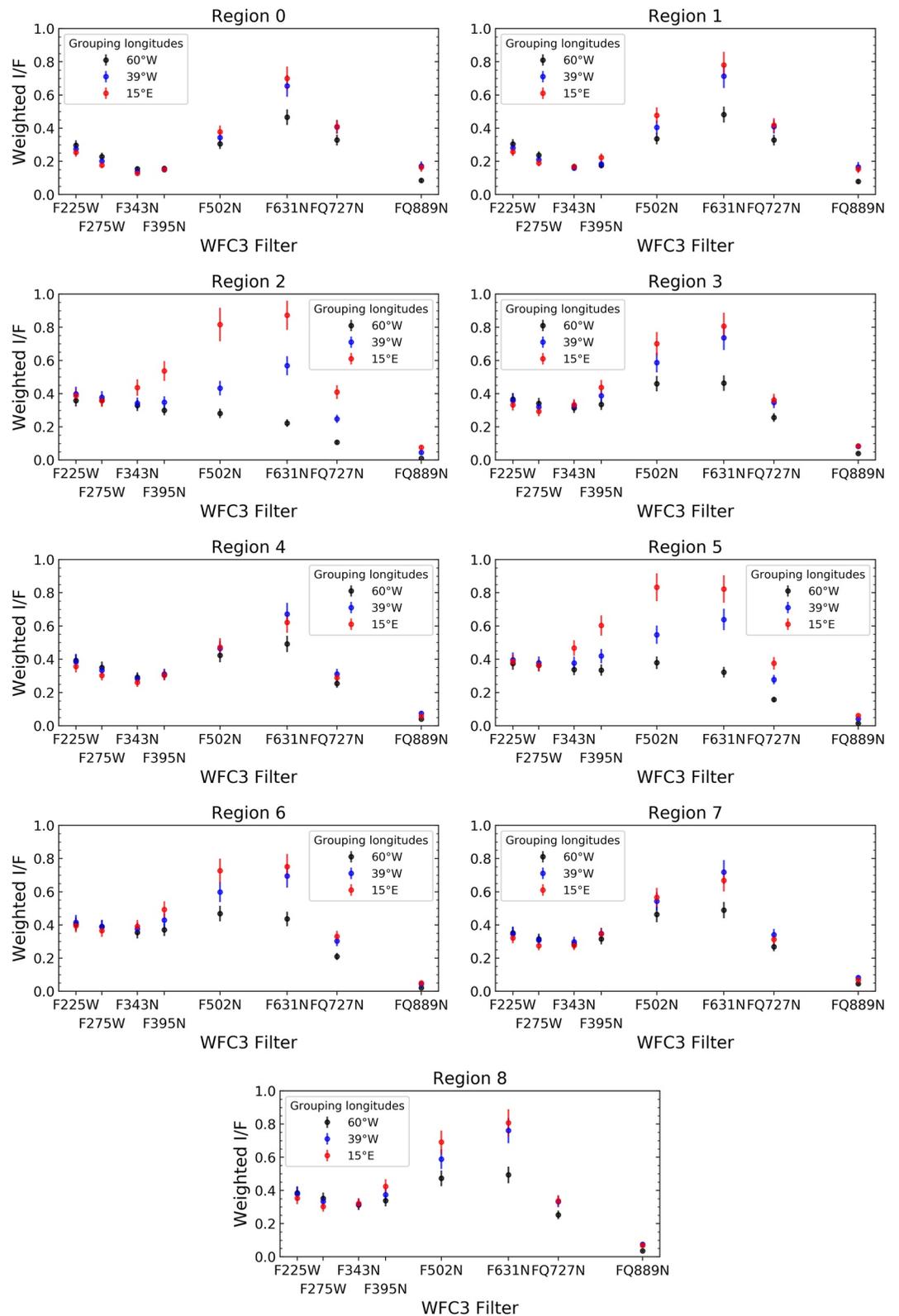
Figure 2. Spectra of the studied regions for three different observing geometries. The grouping longitudes are given relative to the to the sub-observer longitude (Central Meridian).
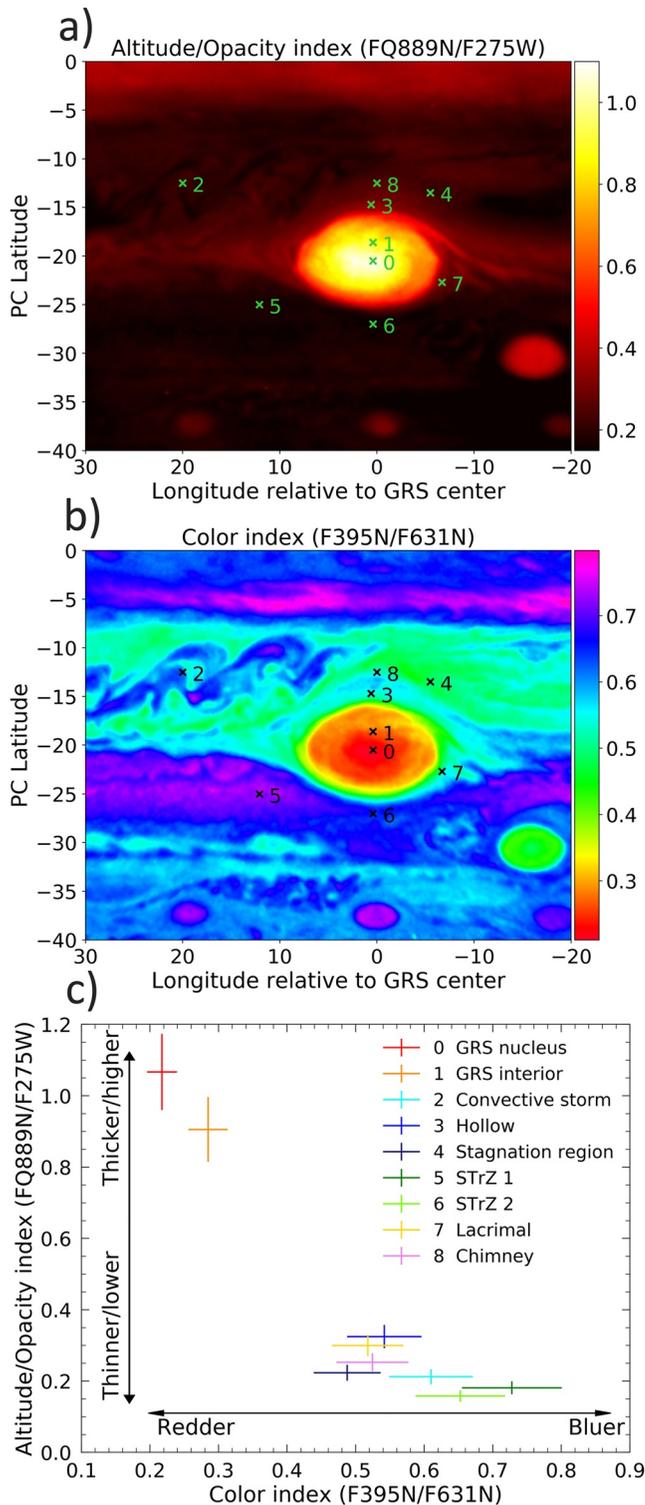
Figure 3. (a and b) Altitude/Opacity Index (AOI) and Color Index (CI) maps made from corrected cropped planispheres. The crosses show the selected regions for radiative transfer analysis. (c) AOI versus CI diagram showing the indices values of the selected regions.

close to the GRS and at latitude 20°S, even if the STrZ values are slightly lower. The CI map indicates that the STrZ together with the southern part of the Equatorial Zone (EZ) are the whitest areas in the cropped planispheres, without considering the ovals present in the South Temperate Belt (STB). At the same time, the areas surrounding the red oval exhibit intermediate CI values and they are not clearly white nor red, but brownish. Regarding the turbulent area west of the GRS, the highest CI values are found in the convective storms, but they do not show a significant deviation in terms of AOI when compared to the background clouds.

In order to give a physically sound interpretation of these indices, we made a very simple atmospheric model with a semi-infinite cloud embedded in an atmosphere including methane absorption and Rayleigh scattering by H_2 and He (Figure S4 in Supporting Information S1). Even if there is a slight dependence on altitude, we found that the CI depends almost exclusively on the Single Scattering Albedo (SSA) at 395 nm. Therefore, it is possible to estimate this parameter from the CI alone. However, AOI depends on cloud altitude and also on SSA(275 nm). Hence, if the SSA(275 nm) is known (or assumed), it is possible to estimate the altitude of the clouds/hazes in a region from the measured AOI (Figure S4 in Supporting Information S1).

3.4. Spectral Clustering

The photometric indices (3) and (4) are a fast and intuitive way to classify the various regions of Jupiter. Other different techniques have been used to spectrally classify various regions of Jupiter, such as the Principal Component Analysis or PCA (Ordonez-Etxeberria et al., 2016; Simon-Miller et al., 2001a, 2001b) or the analysis carried out by Thompson (1990). We use here another method to classify the various regions of Jupiter depending on their spectral brightness: the *k*-means clustering method (Jancey, 1966; Pérez-Hoyos, Sanz-Requena, Sánchez-Lavega, et al., 2012). Using a *k*-means algorithm (Sculley, 2010) the spectra at each pixel of the cropped planispheres are classified depending on their spectral similarity in six clusters, as chosen by visual inspection. The planispheres were corrected following a Minnaert law and the resulting clustering can be found in Figure 4.

A straightforward feature when looking at Figure 4 is that the red oval is different from the rest of the regions, as expected from Figure 3. At the same time, the EZ and the STrZ are both grouped in a similar way, which is reasonable because they both present white regions. This is also the case for the convective storms northwest of the GRS, which are sorted together with the EZ and the STrZ. On the other hand, the background clouds surrounding the convective storms present very dark areas, and so they are grouped with the rest of dark clouds areas, including the south SEB. The "hollow" and the "chimney" also share the same cluster. The "lacrimal" region is classified alone, in a cluster that includes part of the hollow, areas of the SEB and the STB and the reddish oval located approximately at 30°S.

This clustering will allow extrapolating the properties of the selected regions to other areas of the map that are similar enough to be classified together, as will be shown in Section 5.
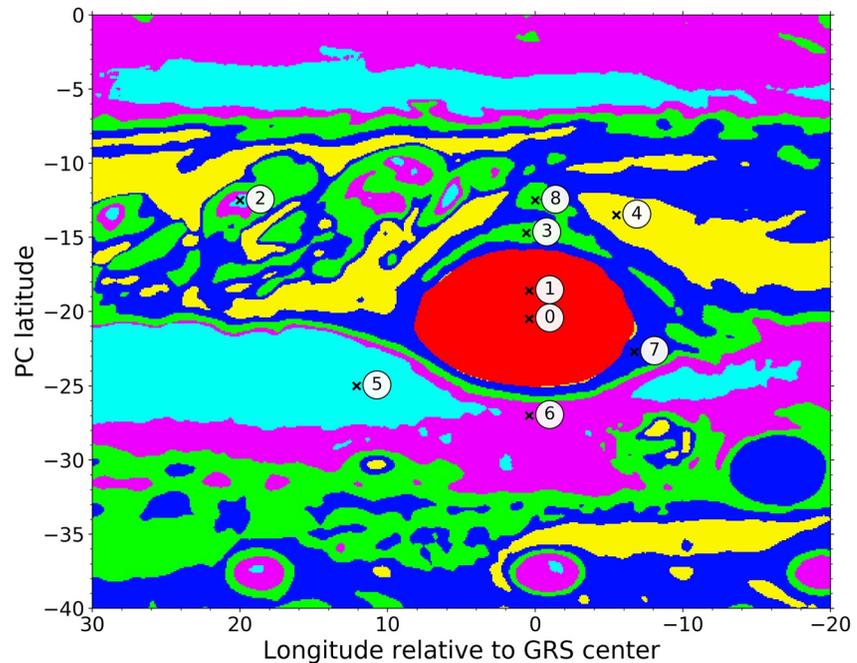
Figure 4. Spectral clustering of the studied area surrounding the Great Red Spot. The black crosses show the selected regions. The colors indicate the clusters found via the k-means algorithm (Sculley, 2010).

4. Radiative Transfer Modeling

We use the NEMESIS radiative transfer suite (Irwin et al., 2008) in order to retrieve atmospheric parameters from the observed spectra as in our previous works (Pérez-Hoyos et al., 2018, 2020; Sanz-Requena et al., 2019; Irwin et al., 2021). NEMESIS is initiated from an *a priori* model atmosphere divided in homogeneous layers to obtain synthetic spectra from the multiple scattering calculations on each layer by means of the doubling-adding technique (Hansen & Travis, 1974). The most likely atmospheric parameters are retrieved after an iterative process that minimizes the differences between the observed and simulated spectra under the optimal estimation scheme (C. D. Rodgers, 2000). We use the correlated-k method (Lacis & Oinas, 1991) to account for methane absorption bands, whose absorption coefficients were taken from Karkoschka and Tomasko (2010).

The atmosphere is divided in 32 layers with altitudes ranging from -20 to 140 km with respect to the 1 bar pressure level (i.e., from 2 bar to 1 mbar). The atmospheric gaseous composition is assumed to be a mixture of H_2, He and CH_4 as given in Taylor et al. (2004).

4.1. *A Priori* Model Atmosphere

We launched a wide range of *a priori* models in order to fit the spectra of five regions (with an area of $0.5° \times 0.5°$) along different longitudes in the South Tropical Zone (Figure S5 in Supporting Information S1).

The grid of *a priori* values of the parameters used for this case is shown in Table 1. We parameterize the vertical distribution of stratospheric and tropospheric hazes with three magnitudes: the bottom pressure (P_{bot}), the peak abundance (N_{peak}) and the ratio of the aerosol to the gas scale heights (fsh). We also set as free parameters the particle mean effective radius r_{eff} and the imaginary part of the refractive index m_i. The real part of the refractive index is computed by means of the Kramers-Kronig relation (Lucarini et al., 2005). The bottom cloud (presumably formed by NH_3) is defined by a factor that scales a previously defined abundance step-like profile.

Table 1
Range of Values of the Parameters Used in the a Priori Atmospheric Model

Layer	Parameter	Type	*A priori* values
Stratospheric haze	P_{bot} [a]	Free	$110^{+240}_{-80}/50^{+180}_{-40}/10^{+100}_{-10}$ mbar
	N_{peak}	Free	$5.5\text{E-}03/0.011/0.022 \pm 0.5$ particles/g
	fsh	Free	$1.0 \pm 0.5/0.1 \pm 0.1$
	m_i [a]	Free	$10^{-3}/m_i\,\text{str}_1/m_i\,\text{str}_2$
	m_r [a] (900 nm)	Fixed	1.65
	r_{eff} [a]	Free	0.3 ± 0.2 μm
	σ_{eff}	Fixed	0.1 μm
Tropospheric haze	P_{bot} [b]	Free	$490^{+230}_{-170}/980^{+220}_{-190}/220^{+160}_{-100}$ mbar
	N_{peak}	Free	$15 \pm 5/30 \pm 5/60 \pm 10$ particles/g
	fsh	Free	$1.0 \pm 0.5/0.1 \pm 0.1$
	m_i [b]	Free	$\text{NTB}_2/\text{NTB}_2 \bullet 0.1$
	m_r [b] (900 nm)	Fixed	1.43
	r_{eff} [b]	Free	1.0 ± 0.5 μm
	σ_{eff}	Fixed	0.1 μm
Bottom cloud	P_1 [b]	Fixed	770 mbar
	P_2 [b]	Fixed	1,000 mbar
	τ_{cld}	Free	$0.1 \pm 1.0/100 \pm 100$
	m_r, m_i	Fixed	Martonchik et al. (1984)
	r_{eff} [b]	Fixed	5.0 μm
	σ_{eff} [b]	Fixed	0.1 μm

Note. Please note that a priori uncertainties in Table 1 are a suggested range for NEMESIS to vary the parameter values in order to fit the data, but the algorithm can go further to provide a good fit.
[a]Zhang et al. (2013). [b]Pérez-Hoyos et al. (2020).

The values of the imaginary refractive indices used as *a priori* are shown in Figure S6 in Supporting Information S1. The curve labeled "Stratospheric m_i 1" is made by interpolating the values given by Zhang et al. (2013) at wavelengths equal to 250 and 900 nm. The curve "Stratospheric m_i 2" is the previous one divided by ten. The "Tropospheric m_i 1" curve is almost equal to the one presented in Pérez-Hoyos et al. (2020), but with a slight reduction of its value at 600 nm following a preliminary analysis. The tropospheric curve with the lower values is again a tenth of the higher one. All the values shown in Table 1 were chosen after an initial non-systematic exploration of the parameter space. Overall, 3,888 different models are covered in Table 1. However, the number of models was increased to 11,664 by exploring two other sets of *a priori* error bars for the imaginary refractive indices.

4.2. Limb-Darkening Analysis

The *a priori* models were evaluated using two different criteria: (a) The overall fit of models and observations at each point and (b) the fit of the measured and modeled limb-darkening with $\left(I/F\right)_0$ and k calculated via Equation 3 (Irwin et al., 2021; Pérez-Hoyos et al., 2020). The first criterion is evaluated in terms of the following error function:

$$\chi^2/N = \frac{1}{N}\sum_{j=1}^{N}\frac{1}{M}\sum_{i=1}^{M}\frac{\left[\left(I/F\right)_{ij}^{\text{obs}} - \left(I/F\right)_{ij}^{\text{mod}}\right]^2}{\left[\Delta\left(I/F\right)_{ij}^{\text{obs}}\right]^2} \tag{4}$$

where N is the number of filters (wavelengths) and M is the number of viewing geometries. $\Delta\left(I/F\right)^{\text{obs}}$ is calculated from the photometric dispersion among the different planispheres of the same filter, the dispersion inside the 5×5 pixels square (Figure 1) and the dispersion among the mean values of the different

squares that have undergone the weighted average (see spectra construction in Section 3.2). However, we set a minimum of 10% for $\Delta\left(I/F\right)^{\mathrm{obs}}$, as this is the typical value in HST/WFC3 absolute calibration (Dressel, 2021). Models with χ^2/N values lower than unity are accepted as good fits to the observed data, although this depends critically on the data uncertainty and the number of free parameters.

We follow the same procedure with the values defining the limb-darkening. Using the logarithmic form of Equation 3 we obtain the $\left(I/F\right)_0$ and k values for each wavelength by performing a linear fit to the points corresponding to the different geometries (Pérez-Hoyos et al., 2020). Then, we define an error function for these magnitudes that covers all the available wavelengths:

$$\left(\chi^2\Big/N\right)_k = \frac{1}{N}\sum_{i=1}^{N}\frac{\left[k_i^{\mathrm{obs}} - k_i^{\mathrm{mod}}\right]^2}{\left[\Delta k_i^{\mathrm{obs}}\right]^2} \tag{5}$$

$$\left(\chi^2\Big/N\right)_{(I/F)_0} = \frac{1}{N}\sum_{i=1}^{N}\frac{\left[\left(I/F\right)_{0,i}^{\mathrm{obs}} - \left(I/F\right)_{0,i}^{\mathrm{mod}}\right]^2}{\left[\Delta\left(I/F\right)_{0,i}^{\mathrm{obs}}\right]^2} \tag{6}$$

The value of the error functions is calculated for all the tested models, and we choose as optimal the one which, having $\chi^2/N < 1$, shows a lower value of $(\chi^2/N)_k + (\chi^2/N)_{(I/F)_0}$. The limb-darkening error functions values for the optimum *a priori* model are shown in Figure 5.

The best-fitting parameter values of this model are given in Table S2 in Supporting Information S1. One noticeable feature of this model is that the retrieved bottom cloud optical depth is well below unity. However, we are not sensitive to the scattered light at those pressure levels, since this model assumes that most of the light extinction in our wavelength range occurs at higher levels. At the same time, our criteria clearly suggest the presence of two coloring agents, as shown by the imaginary refractive indices in Figure 6.

4.3. Retrieval of Selected Regions

The model presented in the previous section was used as the *a priori* model for the radiative transfer analysis of the spectra shown in Figure 2. The retrieved parameter values are shown in Table 2, where we also include the pressure at which the aerosol opacity at 900 nm equals to unity, a proxy to the expected sounding level at each region. The stratospheric and tropospheric bottom pressures (around 110 and 500 mbar, respectively) show few variations from region to region, and are thus not included. Table S3 in Supporting Information S1 shows the improvement factors (Irwin et al., 2015) of the free parameters retrieved in the GRS nucleus (region 0), as a measure of the information gain on each parameter. An improvement factor closer to 1 implies a more substantial reduction of the uncertainty in the considered parameter value.

For all the analyzed regions, we got χ^2/N values well below unity, meaning that we have obtained good fits in all the cases. The minimum error function values are in the STrZ regions 5 and 6, as expected since our a priori model atmosphere was developed using STrZ spectra.

Figure 7 shows the optical depth of the upper hazes and its accumulated vertical profile, as well as the width of the layer between the $\tau_{\mathrm{aer}}(900\,\mathrm{nm}) = 0.5$ and $\tau_{\mathrm{aer}}(900\,\mathrm{nm}) = 2$ pressure levels. As can be deduced from Figure 7, the GRS is located higher in the atmosphere and it is more concentrated when compared to its surroundings. This is in agreement with the AOI indices shown in Figure 3. We include in Figure S4 in Supporting Information S1 the CI and AOI values resulting from these models in comparison to the simpler model explained in Section 3.3.

5. Interpretation of the Results

5.1. Chromophore Nature and Distribution

The retrieved imaginary refractive indices corresponding to the studied regions are shown in Figure 8. The different stratospheric and tropospheric curves clearly suggest the presence of two different coloring agents, both playing a different role in the ultraviolet-blue absorption, in contrast to the universal chromophore
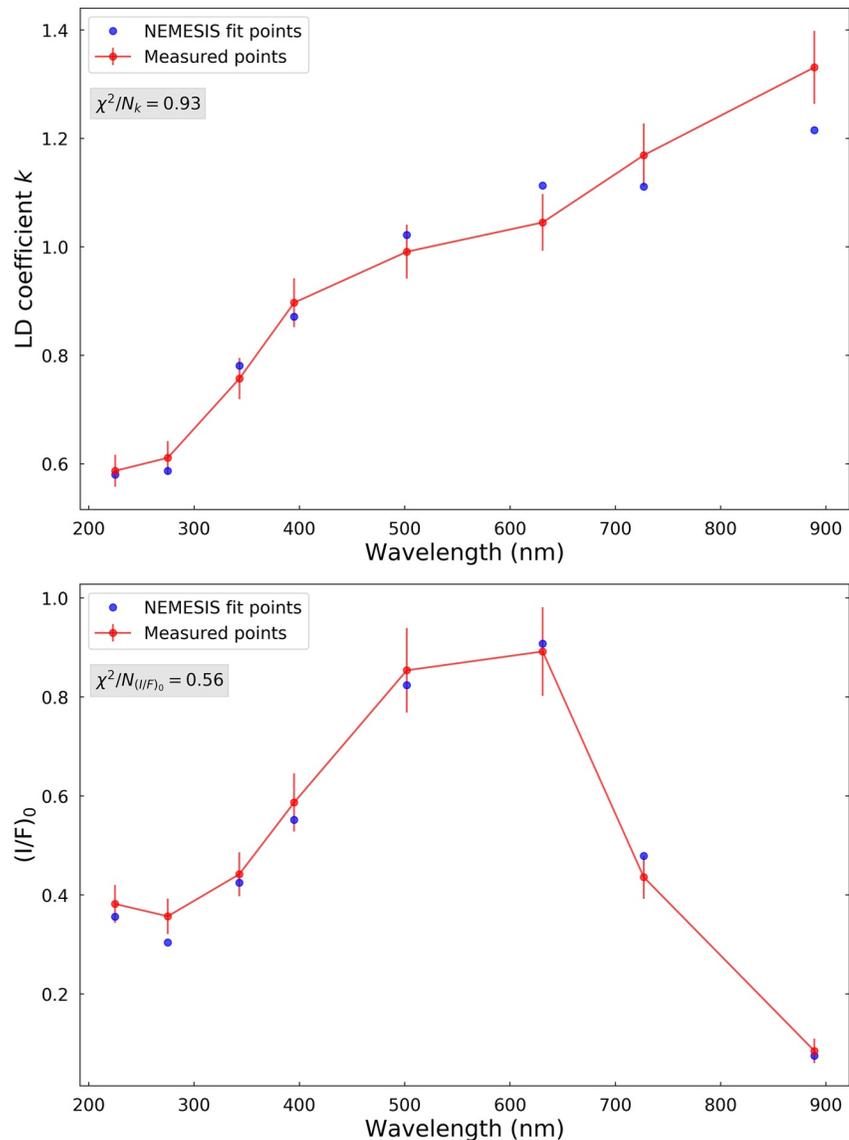
Figure 5. Limb darkening parameter (upper panel) and nadir-viewing reflectivity (lower panel) as a function of wavelength corresponding to the optimal *a priori* model, having the lowest $(\chi^2/N)_k$ and $(\chi^2/N)_{(I/F)_0}$ values indicated in the text boxes. Error bars in the upper panel are obtained from least squares fitting and we set a minimum error of 5%. The origin of $(I/F)_0$ error bars is photometric dispersion (see text).

scheme proposed by Sromovsky et al. (2017). We tried a non-absorbing stratospheric haze (Table 1) when developing the *a priori* model in the STrZ and it did not work properly, even though the STrZ is a "white" region. We also tried two models for region 0 with only tropospheric cloud and the m_i curves of Figure 6 (one model for each m_i curve), and we obtained substantially worse fits than ours. This two-chromophore scheme is in agreement with the PCA analysis performed in Simon-Miller et al. (2001a) and Ordonez-Etxeberria et al. (2016). However, the overall slopes in the 343–500 nm range are higher in the stratospheric than in the tropospheric haze, meaning that the chromophore located at higher levels is more blue absorbing than the lower one. In Figure 8 we also show the imaginary refractive index of the chromophore proposed by Carlson et al. (2016) and its slope in the 400–500 nm range. The slope of Carlson's et al. chromophore is in reasonable agreement with our values, although we find slightly lower slopes, contrary to the results of Braude et al. (2020). Our lower m_i values could be explained by the mixture of the chromophore with low-absorbing aerosols in the atmosphere, which increases the scattering and results in a general decrease of the measured absorption. This is an interesting result, since our starting point was not the one proposed
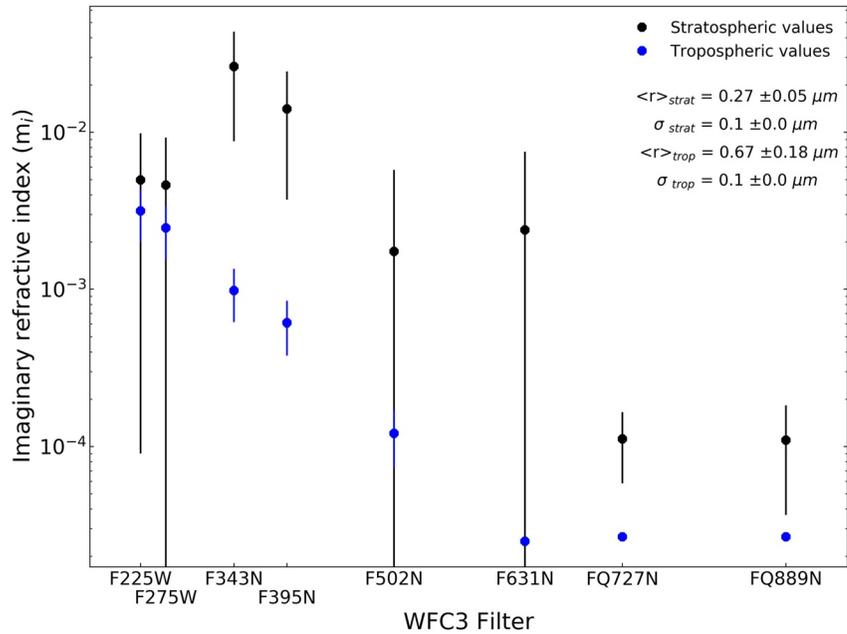
Figure 6. Imaginary refractive indices corresponding to the optimal *a priori* model derived from spectra corresponding to five regions along different longitudes in the STrZ (Figure S5 in Supporting Information S1). Both the stratospheric and tropospheric hazes play a role in the Jovian coloration.

by Carlson et al. (2016). By applying the absorption spectrum of the Carlson et al. (2016) chromophore to the stratospheric haze in our model we obtained a good fit of the region 0 spectra ($\chi^2/N = 0.92$) and a moderate fit of the region 1 spectra ($\chi^2/N = 1.73$) for $\lambda > 0.34$ µm. However, our model fits better the region 0 and region 1 spectra, with $\chi^2/N = 0.67$ and $\chi^2/N = 0.53$, respectively.

Sromovsky et al. (2017) and Baines et al. (2019) proposed the "Crème Brûlée" chromophore model from the analysis of Cassini/VIMS spectra. That model assumes a single chromophore located in a thin layer on top of the optically thick tropospheric cloud as a thin layer. Our results remain on an intermediate level between the "Crème Brûlée" and an extended chromophore scheme (Pérez-Hoyos et al., 2020). We find the upper chromophore to be located near the top of the optically thick tropospheric haze, with its base near the 100 mbar level, higher than the lower 200 mbar bound found by Braude et al. (2020). In addition, Sromovsky et al. (2017) and Baines et al. (2019) found optical depths at 1 µm in the 0.1–0.2 range, while we get much higher values. At the same time, we obtain slightly larger mean effective radii ($r_{eff} \approx 0.3$ µm) when

Table 2
Retrieved Parameter Values for the Studied Regions

| Region	χ^2/N	Stratospheric haze			Tropospheric haze			
		r_{eff} (µm)	Fsh	τ(900 nm)	r_{eff} (µm)	fsh	τ(900 nm)	$P\,(\tau = 1)$ (mbar)
0	0.67	0.29 ± 0.07	0.08	1.8 ± 0.6	2 ± 1	0.34	30 ± 20	75
1	0.53	0.33 ± 0.06	0.14	2.5 ± 0.7	0.7 ± 0.5	0.25	40 ± 30	68
2	0.78	0.27 ± 0.06	0.07	0.8 ± 0.3	0.52 ± 0.07	0.31	25 ± 10	115
3	0.48	0.31 ± 0.07	0.08	0.9 ± 0.3	0.6 ± 0.1	0.32	30 ± 15	107
4	0.54	0.29 ± 0.06	0.09	1.0 ± 0.4	2 ± 1	0.28	6 ± 2	119
5	0.37	0.32 ± 0.03	0.08	0.6 ± 0.2	0.7 ± 0.1	0.27	40 ± 30	139
6	0.28	0.30 ± 0.04	0.08	0.7 ± 0.2	0.7 ± 0.2	0.23	30 ± 20	176
7	0.45	0.29 ± 0.06	0.08	0.9 ± 0.3	0.7 ± 0.2	0.32	20 ± 10	97
8	0.44	0.29 ± 0.04	0.09	0.8 ± 0.2	1.3 ± 0.7	0.26	15 ± 5	156
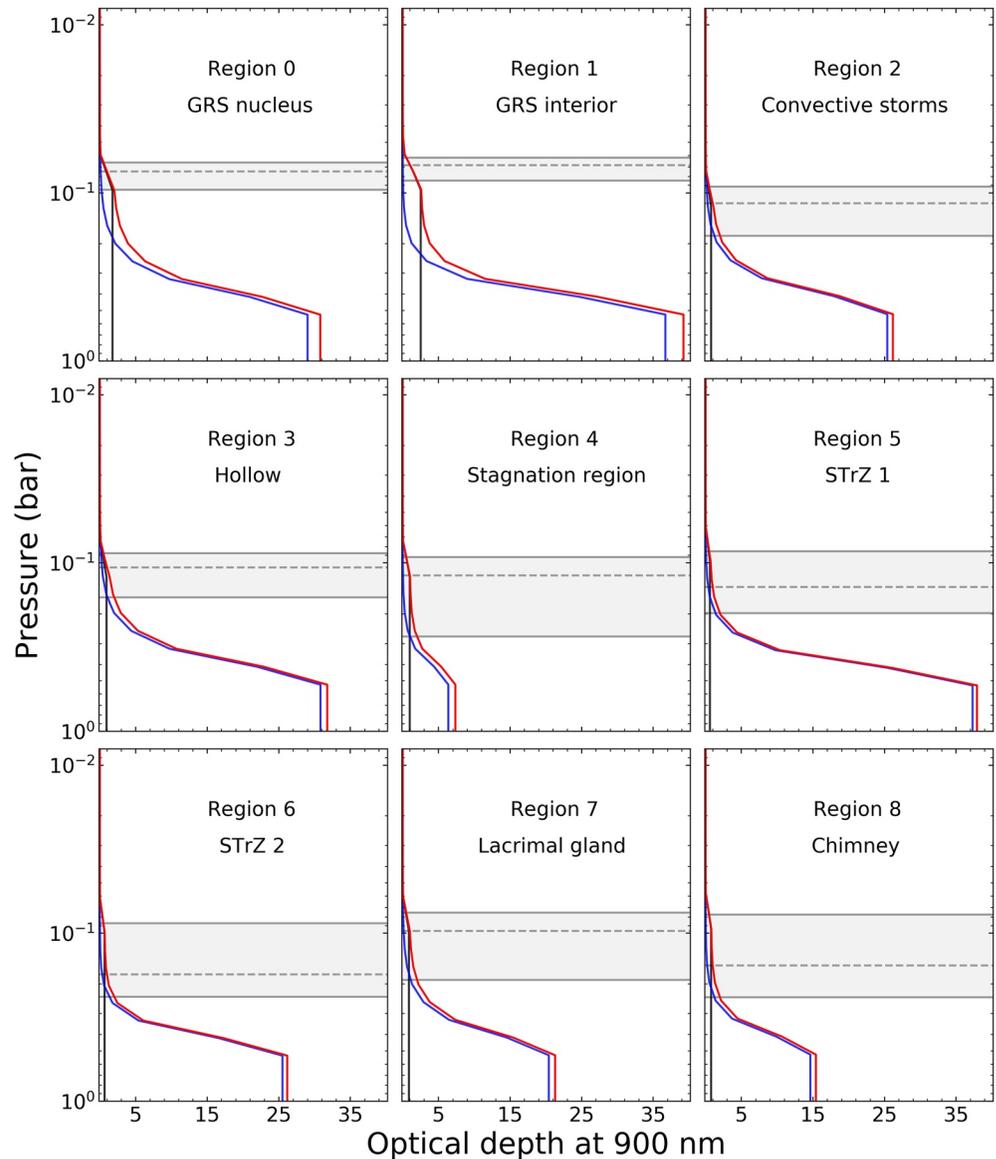
Figure 7. Accumulated optical depth as a function of altitude (pressure). The black, blue and red lines represent the stratospheric, tropospheric and total aerosol optical depths, respectively. The upper and lower gray lines mark the $\tau_{aer}(900 \text{ nm}) = 0.5$ and $\tau_{aer}(900 \text{ nm}) = 2$ pressure levels. The dashed line marks the $\tau_{aer}(900 \text{ nm}) = 1$ pressure level.

compared to those found by Sromovsky et al. (2017) and Baines et al. (2019) ($r_{eff} = 0.1$–0.2 μm). It must be noted though that these works used data acquired in late 2000 and early 2001, and thus some temporal variability may have occurred. Nevertheless, the mass column densities in the GRS interior (20–30 μg/cm²) are in good agreement with the Baines et al. (2019) values (30–40 μg/cm²). In particular, the column mass densities of the "Crème Brûlée" model and region 1 match at a value of approximately 30 μg/cm².

5.2. Altitude and Particle Size

In Figure 9, we show an altitude map with the pressure levels where the total aerosol optical haze reaches unity. The maps in Figure 9 are built by extrapolating the properties retrieved in one region to the areas that are classified within the same spectral cluster (Figure 4). From the altitude map, we find again that the GRS is located higher in the atmosphere than the rest of the regions, as expected from the AOI map in Figure 3. More precisely, we obtain an altitude difference of 14 km between the GRS nucleus and the STrZ.
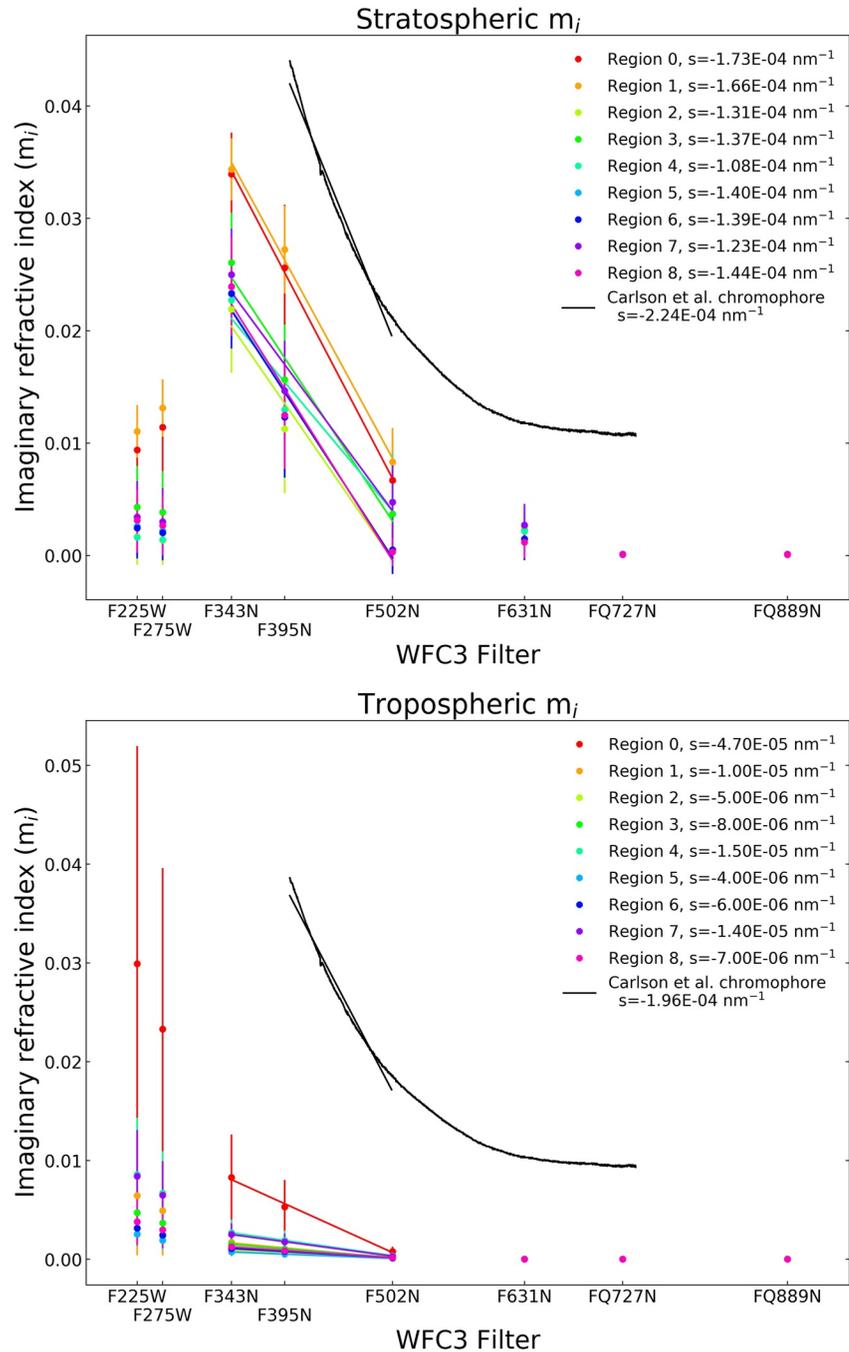
Figure 8. Retrieved imaginary refractive indices and spectral slopes *s* for all the studied regions with a comparison with Carlson's et al. (2016) laboratory chromophore (black lines).

The retrieved altitudes relative to the 1 bar pressure level show a slight disagreement (by about 8 km) with the altimetry map given by Carlson et al. (2016) based on Galileo/NIMS observations at wavelengths close to 2 μm. However, we get similar values when extrapolating our retrieved optical depths to the wavelength range used in that work. We find greater discrepancies with the results given by Grassi et al. (2021), even using their wavelength (2.7 μm) to define the effective cloud top altitude we obtain about a half of the value found in that work for the altitude differences.
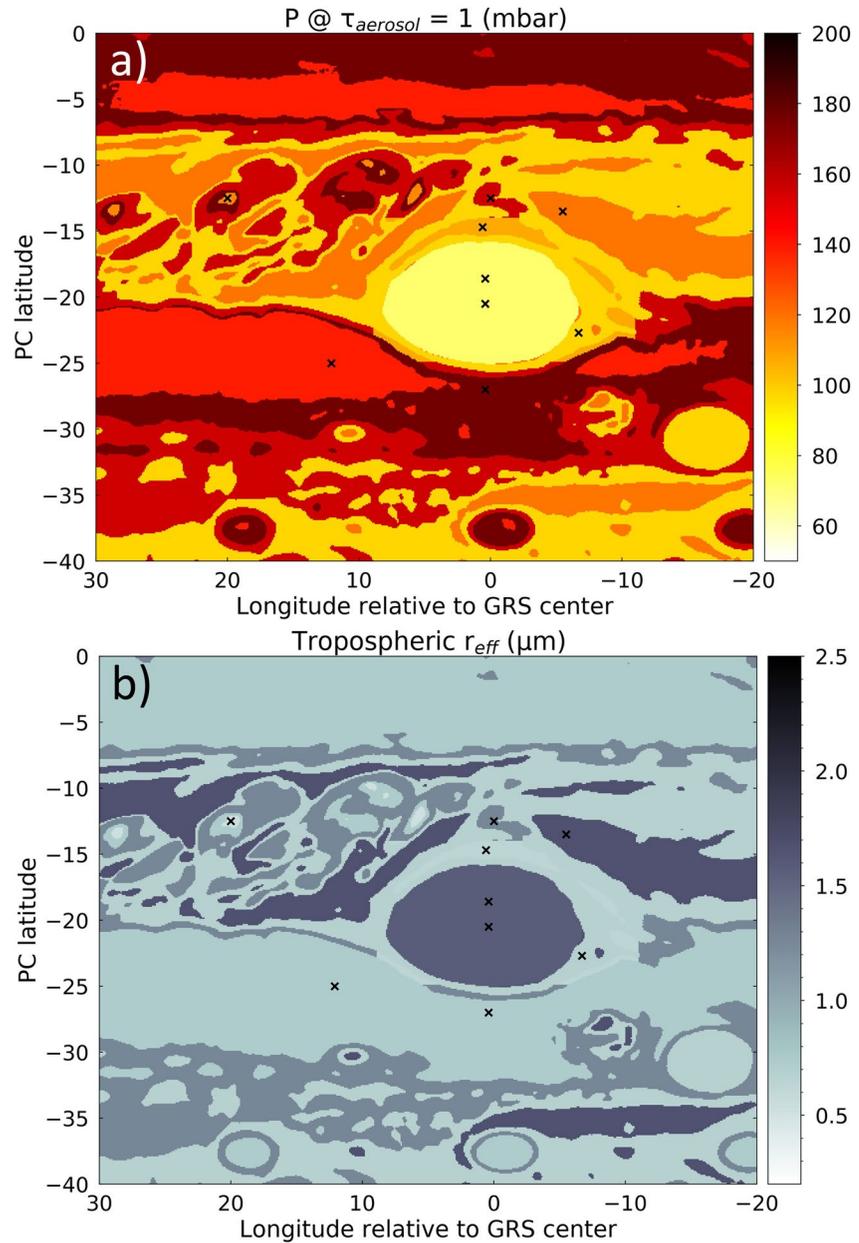
Figure 9. (a) Map showing the pressure levels (in mbar) where the optical depth at 900 nm equals unity. This map can also be interpreted as the cloud top effective altitude. (b) Map showing the mean effective radii (in microns) of tropospheric particles.

In Figure 9 we also show a map of the mean effective radii we retrieve of the tropospheric particles. The mean particle size in the red oval is of 1.6 μm, and it is assumed to be the average of the retrieved radius in the GRS nucleus and interior (regions 0 and 1). This particle size, together with 1.7 μm particles in the stagnation region (region 4), are the biggest particle sizes found in the current analysis.

5.3. Comparison With Previous GRS Models

De Pater et al. (2010) proposed an atmospheric model for the GRS with three haze layers above an optically thick NH_3-ice cloud. The higher haze layer is located in the 2–200 mbar pressure range, and when comparing this haze to our retrieved stratospheric values we find similar values of particle radius and optical depth. The two following haze layers (200–650 and 650–700 mbar) present smaller particle radii and lower optical

depths than our retrieved tropospheric haze in the GRS nucleus (region 0). However, the particle radius of the tropospheric haze in the GRS red oval (region 1) is in good agreement with the particle radius of the haze layer located on top of the NH_3-ice cloud. It is important to note that a significant fraction of light extinction in the de Pater's et al. model takes place in the NH_3-ice cloud, which plays no role in our model and, therefore, higher optical depths in the upper levels are to be expected.

Baines et al. (2019) study of the GRS found the main cloud to have a particle size near 1.6 μm for their stratospheric chromophore model, quite consistent with this study. However, they favored the "Crème Brûlée" model with the chromophore attached to the main cloud. In that model, the mean particle size for the main cloud was of 1.1 μm, which is still comparable to our results. Nevertheless, it must be noted that in both models the tropospheric cloud extends to higher pressure levels (3–4 bar) and the stratospheric haze is located higher (0.04 bar) when compared to our results.

Sánchez-Lavega et al. (2021) included a radiative transfer analysis of both the red oval and a detached portion of reddish material (or flake). We have checked that the model used in Sánchez-Lavega et al. (2021) and the one applied in this work for the GRS interior are compatible. However, we found a better fitting of limb-darkening using our description. When applying our model to their GRS and flake spectra, we get comparable results, as our tropospheric haze considerably reduces its optical depth in the flake to about a half of its value in the GRS interior. Therefore, the hypothesis that the flakes phenomena is a surface phenomenon affecting the higher atmospheric levels (above the 1–2 bar level) is not refuted.

6. Conclusions

In this work, we have presented a radiative transfer analysis of Jupiter's GRS and surroundings using HST/WFC3 images obtained in 2016, covering the spectral range from the UV (225 nm) to the near-infrared (900 nm). We selected and studied nine different regions according to their cloud morphology and spectral diversity. About 12,000 models were explored in order to obtain an *a priori* description of the South Tropical Zone atmosphere. The model showing the best simultaneous fit of both the spectra and their limb-darkening was chosen as the optimal reference for the rest of selected regions. Our main conclusions are:

- All the atmospheric models have three different layers: (a) a stratospheric haze with its base at 100 mbar and particles of 0.3 μm and optical depths of the order of unity, (b) an optically thick ($\tau \sim 10$) tropospheric haze based at 500 mbar with micron sized particles. We are insensitive to a possible cloud deck base.
- We have determined the cloud top altitudes in the GRS (level with optical depth 1 at 900 nm). Our results agree with those of Carlson et al. (2016) though we find differences in relative altitudes with the results of Grassi et al. (2021). For the GRS nucleus, we obtain an altitude difference of 14 km relative to the STrZ, that is, about one scale height.
- For the stratospheric haze, the retrieved imaginary refractive index curves seem to be compatible with the chromophore proposed by Carlson et al. (2016). Our overall lower values may be explained by the mixture of the chromophore with non-absorbing material present high in the atmosphere.
- We also retrieve the wavelength-dependent imaginary refractive index curves of the tropospheric haze. Our work points to the existence of two ultraviolet-blue-absorbing chromophores to explain the coloration of the clouds and hazes in the GRS area. This is in agreement with the conclusions deduced from PCA performed in Simon-Miller et al. (2001a) and Ordonez-Etxeberria et al. (2016). At the same time, it is in disagreement with the 0.35–1.05-μm spectral study of the core of the GRS by Baines et al. (2019), who found excellent fits to the GRS using only the Carlson et al. (2016) chromophore. This may have been because they do not reach to the 0.25 μm region where the tropospheric chromophore found in this study contributes significantly, as suggested by the increasingly high values of the tropospheric haze imaginary refractive index for $\lambda < 350$ nm. Our limb-darkening considerations may have also played a role in favoring the two-chromophore scheme.

The results shown in this work indicate that there is a large spatial variability in the vertical cloud structure among the regions surrounding the GRS. Furthermore, the GRS has proven to suffer considerable color changes between different years (Simon et al., 2018). Because of this, an analysis on a longer time basis is required for a more complete description of the vertical cloud and aerosol structure in the GRS area. This

study will be addressed in a future paper, in which will extend the methodology used here to the HST images covering the time period between 2015 and 2021.

Data Availability Statement

Repository with the data of the figures shown in the main text and supplementary information: Anguiano-Arteaga et al. (2021) http://doi.org/10.5281/zenodo.5084616 Link to download HST program GO 14661 images: https://www.stsci.edu/cgi-bin/get-proposal-info?id=14661&observatory=HST NEMESIS/Radiative transfer code software: Irwin, P. (2020). https://doi.org/10.5281/zenodo.4303976

References

Anguiano-Arteaga, A., Pérez-Hoyos, S., Sánchez-Lavega, A., Sanz-Requena, J. F., & Irwin, P. G. J. (2021). *Vertical distribution of aerosols and hazes over Jupiter's Great Red Spot and its surroundings in 2016 from HST/WFC3 imaging V2*. https://doi.org/10.5281/zenodo.5084616

Baines, K. H., Sromovsky, L. A., Carlson, R. W., Momary, T. W., & Fry, P. M. (2019). The visual spectrum of Jupiter's Great Red Spot accurately modeled with aerosols produced by photolyzed ammonia reacting with acetylene. *Icarus*, *330*, 217–229. https://doi.org/10.1016/j.icarus.2019.04.008

Braude, A. S., Irwin, P. G. J., Orton, G. S., & Fletcher, L. N. (2020). Colour and tropospheric cloud structure of Jupiter from MUSE/VLT: Retrieving a universal chromophore. *Icarus*, *338*, 113589. https://doi.org/10.1016/j.icarus.2019.113589

Carlson, R. W., Baines, K. H., Anderson, M. S., Filacchione, G., & Simon, A. A. (2016). Chromophores from photolyzed ammonia reacting with acetylene: Application to Jupiter's Great Red Spot. *Icarus*, *274*, 106–115. https://doi.org/10.1016/j.icarus.2016.03.008

de Pater, I., Wong, M. H., Marcus, P. S., Luszcz-Cook, S., Ádámkovics, M., Conrad, A., et al. (2010). Persistent rings in and around Jupiter's anticyclones—Observations and theory. *Icarus*, *210*, 742–762. https://doi.org/10.1016/j.icarus.2010.07.027

Dowling, T. E., & Ingersoll, A. P. (1989). Jupiter's Great Red Spot as a Shallow Water System. *Journal of the Atmospheric Sciences*, *46*, 3256–3278. https://doi.org/10.1175/1520-0469(1989)046<3256:jgrsaa>2.0.co;2

Dressel, L. (2021). *Wide field camera 3 instrument handbook version 13.0*. Baltimore: STScI.

Flasar, F. M., Conrath, B. J., Pirraglia, J. A., Clark, P. C., French, R. G., & Gierasch, P. J. (1981). Thermal Structure and Dynamics of the Jovian Atmosphere 1. The Great Red Spot. *Journal of Geophysical Research*, *86*(A10), 8759–8767. https://doi.org/10.1029/ja086ia10p08759

Gierasch, P. J., Ingersoll, A. P., Banfield, D., Ewald, S. P., Helfenstein, P., Simon-Miller, A., et al., & the Galileo Imaging Team. (2000). Observation of moist convection in Jupiter's atmosphere. *Nature*, *403*, 628–630. https://doi.org/10.1038/35001017

Grassi, D., Mura, A., Sindoni, G., Adriani, A., Atreya, S. K., Filacchione, G., et al. (2021). On the clouds and ammonia in Jupiter's upper troposphere from Juno JIRAM reflectivity observations. *Monthly Notices of the Royal Astronomical Society*, *503*, 4892–4907. https://doi.org/10.1093/mnras/stab740

Hansen, J. E., & Travis, L. D. (1974). Light scattering in planetary atmospheres. *Space Science Reviews*, *16*, 527–610. https://doi.org/10.1007/bf00168069

Hueso, R., Legarreta, J., García-Melendo, E., Sánchez-Lavega, A., & Pérez-Hoyos, S. (2009). The jovian anticyclone BA: II. Circulation and interaction with the zonal jets. *Icarus*, *203*, 499–515. https://doi.org/10.1016/j.icarus.2009.05.004

Hueso, R., Sánchez-Lavega, A., & Guillot, T. (2002). A model for large-scale convective storms in Jupiter. *Journal of Geophysical Research*, *107*, 5075. https://doi.org/10.1029/2001je001839

Ingersoll, A. P., Gierasch, P. J., Banfield, D., Vasavada, A. R., & Galileo Imaging Team, fnm, & the Galileo Imaging Team. (2000). Moist convection as an energy source for the large-scale motions in Jupiter's atmosphere. *Nature*, *403*, 630–632. https://doi.org/10.1038/35001021

Irwin, P. G. J., Dobinson, J., James, A., Toledo, D., Teanby, N. A., Fletcher, L. N., et al. (2021). Latitudinal variation of methane mole fraction above clouds in Neptune's atmosphere from VLT/MUSE-NFM: Limb-darkening reanalysis. *Icarus*, *357*, 114277. https://doi.org/10.1016/j.icarus.2020.114277

Irwin, P. G. J., Teanby, N. A., de Kok, R., Fletcher, L. N., Howett, C. J. A., Tsang, C. C. C., et al. (2008). The NEMESIS planetary atmosphere radiative transfer and retrieval tool. *Journal of Quantitative Spectroscopy and Radiative Transfer*, *109*, 1136–1150. https://doi.org/10.1016/j.jqsrt.2007.11.006

Irwin, P. G. J., Tice, D. S., Fletcher, L. N., Barstow, J. K., Teanby, N. A., Orton, G. S., & Davis, G. R. (2015). Reanalysis of Uranus' cloud scattering properties from IRTF/SpeX observations using a self-consistent scattering cloud retrieval scheme. *Icarus*, *250*, 462–476. https://doi.org/10.1016/j.icarus.2014.12.020

Jancey, R. C. (1966). Multidimensional group analysis. *Australian Journal of Botany*, *14*, 127–130. https://doi.org/10.1071/bt9660127

Karkoschka, E. (1998). Methane, Ammonia, and Temperature Measurements of the Jovian Planets and Titan from CCD–Spectrophotometry. *Icarus*, *133*, 134–146. https://doi.org/10.1006/icar.1998.5913

Karkoschka, E., & Tomasko, M. G. (2010). Methane absorption coefficients for the jovian planets from laboratory, Huygens, and HST data. *Icarus*, *205*, 674–694. https://doi.org/10.1016/j.icarus.2009.07.044

Lacis, A. A., & Oinas, V. (1991). A description of the correlated k distribution method for modeling nongray gaseous absorption, thermal emission, and multiple scattering in vertically inhomogeneous atmospheres. *Journal of Geophysical Research*, *96*(D5), 9027–9063. https://doi.org/10.1029/90jd01945

Lucarini, V., Saarinen, J. J., Peiponen, K. E., & Vartiainen, E. M. (2005). *Kramers–Kronig relations in optical materials research*. Springer-Verlag Berlin Heidelberg.

Martonchik, J. V., Orton, G. S., & Appleby, J. F. (1984). Optical properties of NH_3 ice from the far infrared to the near ultraviolet. *Applied Optics*, *23*, 541–547. https://doi.org/10.1364/ao.23.000541

Ordonez-Etxeberria, I., Hueso, R., Sánchez-Lavega, A., & Pérez-Hoyos, P. (2016). Spatial distribution of Jovian clouds, hazes and colors from Cassini ISS multi-spectral images. *Icarus*, *267*, 34–50. https://doi.org/10.1016/j.icarus.2015.12.008

Pérez-Hoyos, S., Sánchez-Lavega, A., García-Muñoz, A., Irwin, P. G. J., Peralta, J., Holsclaw, G., et al. (2018). Venus upper clouds and the UV absorber from MESSENGER/MASCS observations. *Journal of Geophysical Research: Planets*, *123*, 145–162. https://doi.org/10.1002/2017je005406

Pérez-Hoyos, S., Sánchez-Lavega, A., Hueso, R., García-Melendo, E., & Legarreta, J. (2009). The Jovian anticyclone BA: III. Aerosol properties and color change. *Icarus*, *203*, 516–530. https://doi.org/10.1016/j.icarus.2009.06.024

Pérez-Hoyos, S., Sánchez-Lavega, A., Sanz-Requena, J. F., Barrado-Izagirre, N., Carrión-González, O., Anguiano-Arteaga, A., et al. (2020). Color and aerosol changes in Jupiter after a North Temperate Belt disturbance. *Icarus*, *132*, 114021. https://doi.org/10.1016/j.icarus.2020.114031

Pérez-Hoyos, S., Sanz-Requena, J. F., Barrado-Izagirre, N., Rojas, J. F., & Sánchez-Lavega, A., & The IOPW Team. (2012). The 2009–2010 fade of Jupiter's South Equatorial Belt: Vertical cloud structure models and zonal winds from visible imaging. *Icarus*, *217*, 256–271. https://doi.org/10.1016/j.icarus.2011.11.008

Pérez-Hoyos, S., Sanz-Requena, J. F., Sánchez-Lavega, A., Wong, M. H., Hammel, H. B., Orton, G. S., et al. (2012). Vertical cloud structure of the 2009 Jupiter impact based on HST/WFC3 observations. *Icarus*, *221*, 1061–1078. https://doi.org/10.1016/j.icarus.2012.10.012

Rodgers, C. D. (2000). Inverse methods for atmospheric sounding: Theory and practice. *World Scientific, Series on Atmospheric, Oceanic and Planetary Physics*, *2*.

Rogers, J. H. (1995). *The giant planet Jupiter* (p. 45). Cambridge University Press.

Rogers, J. H. (2019). *Jupiter in 2019, Report No. 7: Continuing disruption of the GRS*. British Astronomical Association. Retrieved From https://britastro.org/node/18917

Sada, P. V., Beebe, R. F., & Conrath, B. J. (1996). Comparison of the structure and dynamics of Jupiter's Great Red Spot between the Voyager 1 and 2 encounters. *Icarus*, *119*, 311–335. https://doi.org/10.1006/icar.1996.0022

Sánchez-Lavega, A. (2011). *An Introduction to Planetary Atmospheres* (Vol. 38, p. 273). Taylor-Francis, CRC Press.

Sánchez-Lavega, A., Anguiano-Arteaga, A., Iñurrigarro, P., Garcia-Melendo, E., Legarreta, J., Hueso, R., et al. (2021). Jupiter's Great Red Spot: Strong interactions with incoming anticyclones in 2019. *Journal of Geophysical Research: Planets*, *126*, e2020JE006686. https://doi.org/10.1029/2020JE006686

Sánchez-Lavega, A., Hueso, R., Eichstädt, G., Orton, G., Rogers, J., Hansen, C. J., et al. (2018). The rich dynamics of Jupiter's Great Red Spot from JunoCam – Juno images. *The Astronomical Journal*, *156*(9), 162. https://doi.org/10.3847/1538-3881/aada81

Sánchez-Lavega, A., Legarreta, J., García-Melendo, E., Hueso, R., Pérez-Hoyos, S., Gómez-Forrellad, J. M., et al. (2013). Colors of Jupiter's large anticyclones and the interaction of a Tropical Red Oval with the Great Red Spot in 2008. *Journal of Geophysical Research: Planets*, *118*, 2537–2557. https://doi.org/10.1002/2013je004371

Sanz-Requena, J. F., Pérez-Hoyos, S., Sánchez-Lavega, A., del Rio-Gaztelurrutia, T., & Irwin, P. G. J. (2019). Hazes and clouds in a singular triple vortex in Saturn's atmosphere from HST/WFC3 multispectral imaging. *Icarus*, *333*, 22–36. https://doi.org/10.1016/j.icarus.2019.05.037

Sculley, D. (2010). Web Scale K-Means clustering. In *Proceedings of the 19th international conference on World Wide Web*. Retrieved From https://www.eecs.tufts.edu/~dsculley/papers/fastkmeans.pdf

Simon, A. A., Tabataba-Vakili, F., Cosentino, R., Beebe, R. F., Wong, M. H., & Orton, G. S. (2018). Historical and contemporary trends in the size, drift, and color of Jupiter's Great Red Spot. *The Astronomical Journal*, *155*(13), 151. https://doi.org/10.3847/1538-3881/aaae01

Simon, A. A., Wong, M. H., & Orton, G. S. (2015). First results from the Hubble OPAL Program: Jupiter in 2015. *The Astronomical Journal*, *812*, 55. https://doi.org/10.1088/0004-637x/812/1/55

Simon-Miller, A. A., Banfield, D., & Gierasch, P. J. (2001a). An HST study of Jovian chromophores. *Icarus*, *149*, 94–106. https://doi.org/10.1006/icar.2001.6473

Simon-Miller, A. A., Banfield, D., & Gierasch, P. J. (2001b). Color and the vertical structure in Jupiter's belts, zones, and weather systems. *Icarus*, *154*, 459–474. https://doi.org/10.1006/icar.2001.6742

Sromovsky, L. A., Baines, K. H., Fry, P. M., & Carlson, R. W. (2017). A possibly universal red chromophore for modeling color variations on Jupiter. *Icarus*, *291*, 232–244. https://doi.org/10.1016/j.icarus.2016.12.014

Taylor, F. W., Atreya, S. K., Encrenaz, T., Hunten, D. M., Irwin, P. G. J., & Owen, T. C. (2004). The composition of the atmosphere of Jupiter. In Bagenal, F., McKinnon, W., & Dowling, T. (Eds.), *Jupiter: The planet, satellites and magnetosphere* (pp. 59–78). Cambridge University Press..

Thompson, W. R. (1990). Global four-band spectral classification of Jupiter's clouds: Color/albedo units and trends. *The International Journal of Supercomputing Applications*, *4*, 48–65. https://doi.org/10.1177/109434209000400205

Wong, M. H., de Pater, I., Asay-Davis, X., Marcus, P. S., & Go, C. Y. (2011). Vertical structure of Jupiter's Oval BA before and after it reddened: What changed? *Icarus*, *215*, 211–225. https://doi.org/10.1016/j.icarus.2011.06.032

Zhang, X., West, R. A., Banfield, D., & Yung, Y. L. (2013). Stratospheric aerosols on Jupiter from Cassini observations. *Icarus*, *226*, 159–171. https://doi.org/10.1016/j.icarus.2013.05.020